An Improved Tool Path Model Including Periodic Delay for Chatter Prediction in Milling

R. P. H. Faassen[1]
e-mail: r.p.h.faassen@tue.nl

N. van de Wouw

H. Nijmeijer

Department of Mechanical Engineering,
Eindhoven University of Technology,
P.O. Box 513,
5600 MB Eindhoven, The Netherlands

J. A. J. Oosterling
Division of Design and Manufacturing,
TNO Science and Industry,
P.O. Box 6235,
5600 HE Eindhoven, The Netherlands

The efficiency of the high-speed milling process is often limited by the occurrence of chatter. In order to predict the occurrence of chatter, accurate models are necessary. In most models regarding milling, the cutter is assumed to follow a circular tooth path. However, the real tool path is trochoidal in the ideal case, i.e., without vibrations of the tool. Therefore, models using a circular tool path lead to errors, especially when the cutting angle is close to 0 or π radians. An updated model for the milling process is presented which features a model of the undeformed chip thickness and a time-periodic delay. In combination with this tool path model, a nonlinear cutting force model is used, to include the dependency of the chatter boundary on the feed rate. The stability of the milling system, and hence the occurrence of chatter, is investigated using both the traditional and the trochoidal model by means of the semi-discretization method. Due to the combination of this updated tool path model with a nonlinear cutting force model, the periodic solution of this system, representing a chatter-free process, needs to be computed before the stability can be investigated. This periodic solution is computed using a finite difference method for delay-differential equations. Especially for low immersion cuts, the stability lobes diagram (SLD) using the updated model shows significant differences compared to the SLD using the traditional model. Also the use of the nonlinear cutting force model results in significant differences in the SLD compared to the linear cutting force model. [DOI: 10.1115/1.2447465]

Keywords: high-speed milling, stability, finite difference method, tool path, periodic delay differential equations

1 Introduction

High-speed milling is used in many sectors of industry. For example in the aerospace manufacturing industry, large parts are made out of a single workpiece where 90% of the material is removed. Moreover, in the mould making industry high-speed milling is used. Here, as a rule the radial immersion is low as a result of the complex geometries of the workpiece and the difficult machinability of the workpiece material. The material removal rate in milling is often limited by the occurrence of an instability phenomenon called regenerative chatter. Chatter results in heavy vibrations of the tool causing an inferior workpiece surface quality, rapid tool wear and noise.

Research regarding regenerative chatter started in the late 1950s with Refs. [1,2]. They have introduced a stability lobes diagram (SLD), which graphically shows the stability limit as a function of machining parameters, such as spindle speed and depth of cut. The stability of the milling process for low immersion cutting is recently investigated in Refs. [3–7]. In these papers, the focus lies on the impact behavior of the tool hitting the workpiece for a small period of time.

In most models regarding milling, see e.g., Refs. [8,9], the tooth path is modeled as a circular arc. In this paper, we will call this tooth path model the traditional model. Using this model, the undeformed chip thickness is approximated by a sinusoid. However, the path of a milling cutter is trochoidal [10,11], which leads to different equations for the undeformed chip thickness. More accurate models exist compared to the sinusoidal approximation [12–14], but they are not widely used, because of the complex equations involved. However, especially when $\sin\phi(t)$ is small (with $\phi(t)$ the tooth angle at time t), which is often the case in low immersion cutting, the errors using the traditional model are large. Furthermore, using the traditional model it is assumed that for upmilling the entry angle of the cut is $\phi_s=0$ rad and that the exit angle for downmilling is $\phi_e=\pi$ rad. The trochoidal model for the static chip thickness shows that the tool enters the cut somewhat sooner and leaves it somewhat later.

For the prediction of chatter in high-speed milling, not only is the static chip thickness important, but also the dynamic chip thickness, which is due to the regenerative effect. Most often, the dynamic chip thickness is calculated by subtracting the vibrations $\underline{v}(t-\hat{\tau})$ at the time $t-\hat{\tau}$ one tooth passing time earlier from the vibrations $\underline{v}(t)$ at the current time t, see e.g., Refs. [8,15,16]. This results in a delay differential equation (DDE) modeling the milling process. However, as was also shown by Long and Balachandran [17], the delay is not constant, but periodic when the trochoidal tool path is taken into account.

In this paper, the effect of the trochoidal tooth path in combination with a nonlinear cutting force model on the stability is investigated. This will answer the question whether the stability of the milling process, computed using the circular tooth path, differs significantly from the stability of the milling process, computed using the trochoidal tooth path model. For this trochoidal tool path model, an updated equation describing the static chip thickness is derived. Furthermore, the delay is modeled as being periodic instead of constant and equations for the entry and exit angles are formulated. To include the effect of the feed rate on the stability border, nonlinear relations between the chip thickness and cutting force are used [18]. For a nonchatter situation, the system of periodic DDEs describing the milling process has a stable periodic solution, whereas for the case when chatter occurs, this periodic

[1]Corresponding author.

Contributed by the Design Engineering Division of ASME for publication in the Journal of Computational and Nonlinear Dynamics. Manuscript received August 22, 2006; final manuscript received December 11, 2006. Review conducted by David Gilsinn.

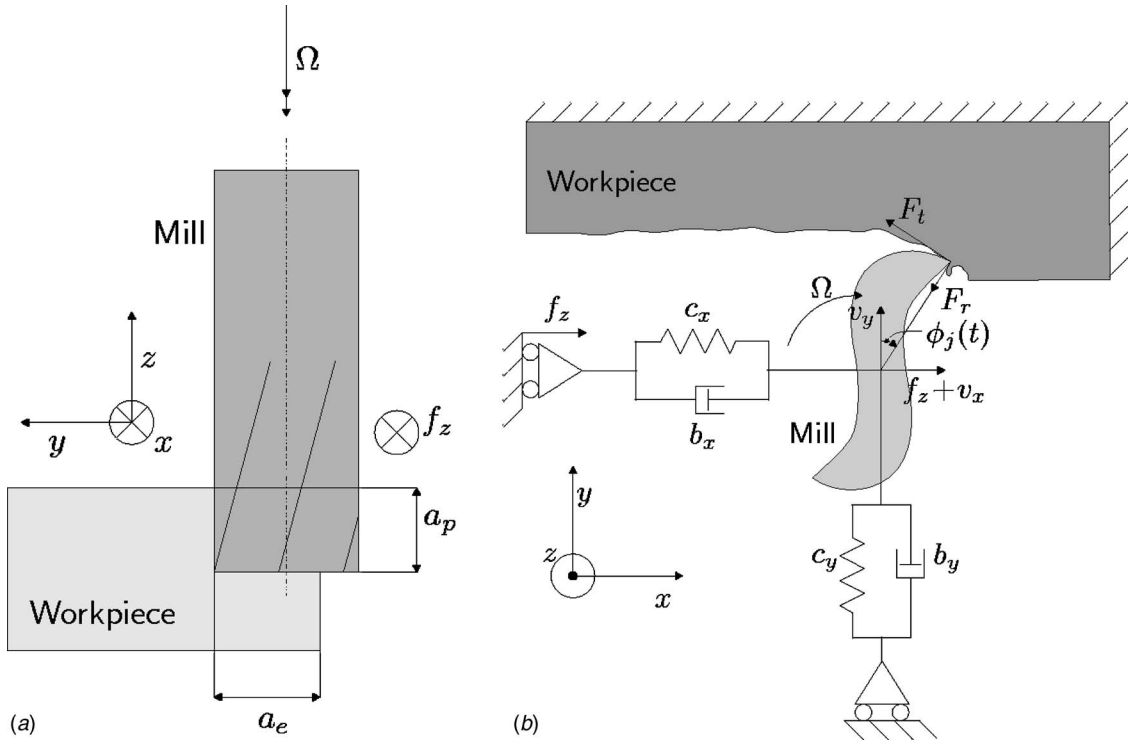

Fig. 1 Schematic representation of the milling process; (*a*) side view, (*b*) top view

solution becomes unstable. Since a nonlinear cutting force model is used in combination with a periodic delay, this periodic solution has to be calculated explicitly. This periodic solution is found using a finite difference scheme. The stability limit of this periodic solution is assessed using the semi-discretization method of Refs. [16,19]. This is a well-known method that can be used to determine the stability of delay differential equations. Especially for low immersion cutting, it is shown that the stability lobes change drastically using the trochoidal model compared with the lobes generated using the traditional model.

The paper is organized as follows: in Sec. 2, the new equations describing the undeformed chip thickness, the delay, and the entry and exit angles are derived and a comparison between different models is provided. In Sec. 3, a finite difference scheme is presented to compute a periodic solution of the model. In Sec. 4, the stability of the new and the traditional model is investigated using the semi-discretization method and discussed in terms of the implications for the milling process in Sec. 5. Finally, conclusions are drawn in Sec. 6.

2 Modeling the Milling Process

A schematic representation of the milling process is shown in Fig. 1 and a block diagram of the model is shown in Fig. 2.

The cutter rotates at a spindle speed Ω and translates in x direction with a certain chip load f_z. The forces that act on tooth j of the cutter are the tangential force $F_{t_j}(t)$ and the radial force $F_{r_j}(t)$

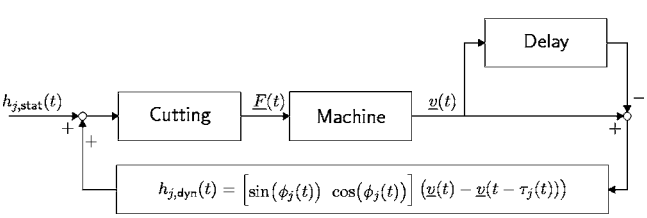

Fig. 2 Block diagram of the milling process

and are a result of the chip thickness $h_j(t)$. Due to the dynamics of the tool, toolholder, and spindle (represented in Fig. 1(*b*) by a linear mass, spring, damper system), the tool displaces in x and y directions by $\underline{v}(t)=[v_x(t)\ v_y(t)]^T$.

The undeformed chip thickness is the sum of the static chip thickness $h_{j,\mathrm{stat}}(t)$ and the dynamic chip thickness $h_{j,\mathrm{dyn}}(t)$

$$h_j(t) = h_{j,\mathrm{stat}}(t) + h_{j,\mathrm{dyn}}(t) \tag{1}$$

The static chip thickness is the part of the chip thickness which is due to the position of the tool that is dictated by the feed and spindle speed. The dynamic chip thickness is the part which is a result of the vibrations of the cutter.

For a two-dimensional case, the static chip thickness is often modeled by

$$h_{j,\mathrm{stat}}(t) = f_z \sin \phi_j(t) \tag{2}$$

where f_z is the chip load and $\phi_j(t)$ is the angle of tooth j at time t. The dynamic chip thickness is often modeled by

$$h_{j,\mathrm{dyn}}(t) = [\sin \phi_j(t)\ \cos \phi_j(t)](\underline{v}(t) - \underline{v}(t-\hat{\tau})) \tag{3}$$

Here the constant time delay is given by

$$\hat{\tau} = \frac{2\pi}{z\Omega} \tag{4}$$

where z is the number of teeth and Ω is the spindle speed in rad/s.

This model assumes a circular tooth path. However, the real tool path is trochoidal (see Fig. 3). In this figure, the chip load is chosen rather unrealistically large to increase readability of the figure. The tool moves in the feed direction x. The meaning of the points defined in the figure are shown in Table 1. Here, $\underline{p}_c(t)$ and $\underline{p}_j(t)$ represent the position of the center of the cutter and the position of tooth $j=0,1,\ldots,z$ at time t, respectively. In Fig. 4, the circular tool path approximation is shown.

The delay $\tau_j(t)$ is defined as the delay that is involved when calculating the chip thickness that tooth j removes at time t. In Fig. 3, $\tau_2(t)$ is the difference between the time when tooth 2 is at

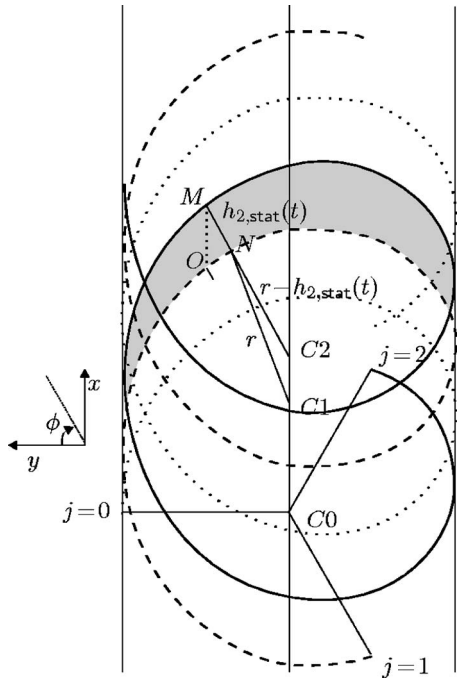

Fig. 3 The tooth path of a mill with three teeth

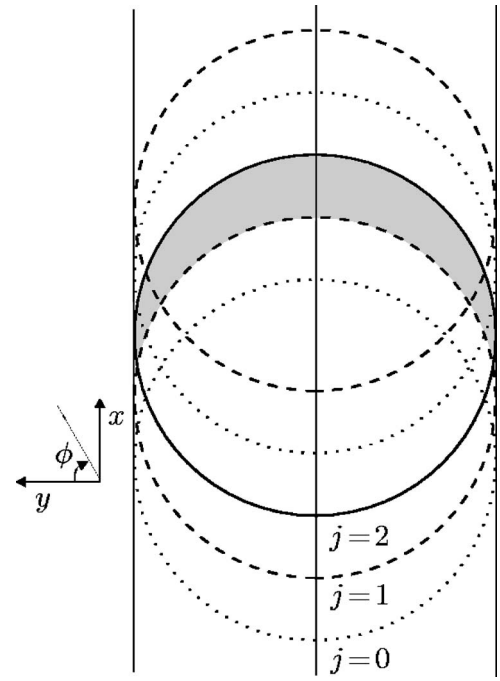

Fig. 4 The circular tooth path approximation of a mill with three teeth

point M and the time when tooth 1 is at point N. Here, the index 2 refers to tooth 2, since this delay is involved when calculating the dynamic chip thickness experienced by tooth 2 at time t. The center of the cutter at time t is at position $C2$. At time $t-\tau_2(t)$, the center is at position $C1$. Note that when applying Eq. (3) with a constant delay $\hat{\tau}$, the vibrations at point O are subtracted from the vibrations at point M to obtain the chip thickness experienced by tooth 2 at time t. However, the dynamic chip thickness is described by the subtraction of the vibrations at point N from the vibrations of point M.

In the sequel, an equation for the static chip thickness is derived for the case of a trochoidal tool path. By doing so, an expression for the delay is also obtained, which can be used to calculate the dynamic chip thickness in a later stage. It should be noted that the vibrations of the cutter are assumed zero for deriving the delay. When vibrations of the tool are taken into account, points M and N move as a result of these vibrations. Hence, the delay also changes and becomes state dependent (see Ref. [20]). As mentioned by those authors, the influence of the state dependent delay on the stability is small. Therefore, and for the sake of simplicity, this is not taken into account here. In Ref. [21], the variation of the delay as a function if the rotation angle is approximated by introducing two separate constant delays in feed and normal direction, respectively.

Table 1 Positions of points of Fig. 3

Point	Position
……	Tooth 0
---	Tooth 1
—	Tooth 2
$C0$	$\underline{p}_c(t=0)$
$C1$	$\underline{p}_c(t-r_2(t))$
$C2$	$\underline{p}_c(t)$
M	$\underline{p}_2(t)$
N	$\underline{p}_1(t-\tau_2(t))$
O	$\underline{p}_1(t-\hat{\tau})$

The position of a point $\underline{p}_j(t)$ on the tip of tooth j at time t can be described as the sum of the position of the center of the cutter $\underline{p}_c(t)=[\phi_0(t)f_z z/(2\pi)\ 0]^T$ at time t and the position of the tip relative to this center. With $\underline{p}_j=[p_{x_j}\ p_{y_j}]^T$, this gives

$$\underline{p}_j(t)=\underline{p}_c(t)+\begin{bmatrix} r\sin\phi_j(t) \\ r\cos\phi_j(t)\end{bmatrix}=\begin{bmatrix} \frac{f_z z}{2\pi}\phi_0(t)+r\sin\phi_j(t) \\ r\cos\phi_j(t)\end{bmatrix} \tag{5}$$

with r the radius of the tool. Here a constant spindle speed Ω and feed per tooth f_z are assumed.

Point N in Fig. 3 can be described as the position of tooth 1 at time $t-\tau_2(t)$. This position is described by

$$\underline{p}_1(t-\tau_2(t))=\begin{bmatrix} \frac{f_z z}{2\pi}\phi_0(t-\tau_2(t))+r\sin\phi_1(t-\tau_2(t)) \\ r\cos\phi_1(t-\tau_2(t))\end{bmatrix} \tag{6}$$

However, it can also be defined as the position of tooth 2 at time t for a tool radius of $r-h_{2,\text{stat}}(t)$. This yields

$$\underline{p}_2(t)=\begin{bmatrix} \frac{f_z z}{2\pi}\phi_0(t)+(r-h_{2,\text{stat}}(t))\sin\phi_2(t) \\ (r-h_{2,\text{star}}(t))\cos\phi_2(t)\end{bmatrix} \tag{7}$$

For an arbitrary tooth j, Eqs. (6) and (7) are, respectively, generalized by

$$\underline{p}_{j-1}(t-\tau_j(t))=\begin{bmatrix} \frac{f_z z}{2\pi}\phi_0(t-\tau_j(t))+r\sin\phi_{j-1}(t-\tau_j(t)) \\ r\cos\phi_{j-1}(t-\tau_j(t))\end{bmatrix} \tag{8}$$

and

$$\underline{p}_j(t)=\begin{bmatrix} \frac{f_z z}{2\pi}\phi_0(t)+(r-h_{j,\text{stat}}(t))\sin\phi_j(t) \\ (r-h_{j,\text{stat}}(t))\cos\phi_j(t)\end{bmatrix} \tag{9}$$

Equating Eqs. (8) and (9) in the y direction gives

$$r\cos\phi_{j-1}(t-\tau_j(t)) = (r - h_{j,\text{stat}}(t))\cos\phi_j(t) \tag{10}$$

where tooth 0 equals tooth z and tooth $j-1$ equals tooth $z-1$. After substitution of

$$\phi_j(t) = \phi_0(t) - j\theta = \Omega t - j\frac{2\pi}{z} \tag{11}$$

with θ the angle between two subsequent teeth

$$\theta = \frac{2\pi}{z} = \hat{\tau}\Omega \tag{12}$$

the chip thickness can be expressed as

$$\begin{aligned} h_{j,\text{stat}}(t)\cos\phi_j(t) &= r\cos\phi_j(t) - r\cos\big(\phi_j(t-\tau_j(t)) + \theta\big) \\ &:= h_y\cos\phi_j(t) \\ &:= A \end{aligned} \tag{13}$$

Similarly, by equating Eqs. (8) and (9) in x direction, another expression for the chip thickness is found

$$\begin{aligned} h_{j,\text{stat}}(t)\sin\phi_j(t) &= \frac{f_z z}{2\pi}\Omega\tau_j(t) + r\sin\phi_j(t) - r\sin\big(\phi_j(t-\tau_j(t)) + \theta\big) \\ &:= h_x\sin\phi_j(t) \\ &:= B \end{aligned} \tag{14}$$

Now, Eqs. (13) and (14) can be used to express the chip thickness. However, if the denominator of any of these equations approaches zero, the right part of this equation tends to $\pm\infty$. Therefore, it will be shown that both equations can be combined to obtain a single equation for the chip thickness that can always be used. Before this expression for the chip thickness can be formulated, first an expression for the time-varying delay should be derived.

2.1 Time Delay. Setting $h_{j,\text{stat}}(t)=h_y=h_x$ and using Eqs. (13) and (14) gives

$$B\cos\phi_j(t) = A\sin\phi_j(t) \tag{15}$$

Substitution of Eqs. (4), (11), (13), and (14) in Eq. (15) and applying trigonometric relations yields

$$\frac{f_z\tau_j(t)}{\hat{\tau}}\cos\phi_j(t) + r\sin\big(\Omega(\tau_j(t)-\hat{\tau})\big) = 0 \tag{16}$$

Since the contribution of the trochoidal tool path on the delay is small compared to the nominal delay $\hat{\tau}$, the time-varying delay can be regarded as the sum of the constant tooth passing time delay $\hat{\tau}$ and a small time-periodic function $\delta\tau_j(t)$

$$\tau_j(t) = \hat{\tau} + \delta\tau_j(t) \tag{17}$$

with $\delta\tau_j(t+\hat{\tau}) = \delta\tau_{j-1}(t)$. Substitution of Eq. (17) in Eq. (16) gives

$$f_z\cos\phi_j(t) + \frac{f_z\cos\phi_j(t)}{\hat{\tau}}\delta\tau_j(t) + r\sin(\Omega\delta\tau_j(t)) = 0 \tag{18}$$

Since $|\Omega\delta\tau_j(t)| \ll 1$, truncation of the Taylor's series expansion of $\sin[\Omega\delta\tau_j(t)]$ after the first-order term yields $\sin[\Omega\delta\tau_j(t)] \approx \Omega\delta\tau_j(t)$. Using this approximation in Eq. (18) gives an expression for $\delta\tau_j(t)$

$$\delta\tau_j(t) = -\frac{\hat{\tau}f_z\cos\phi_j(t)}{f_z\cos\phi_j(t) + r\Omega\hat{\tau}} \tag{19}$$

The time-varying delay can now be expressed by substituting Eqs. (12) and (19) in Eq. (17) and rearranging terms to obtain

$$\tau_j(t) = \frac{\hat{\tau}\theta r}{f_z\cos\phi_j(t) + \theta r} \tag{20}$$

A similar result was recently found by Long and Balachandran [17], although they used a different approach where no equation for the static chip thickness was derived.

2.2 Chip Thickness. Since the time-varying delay is now known, an expression for the chip thickness can be derived. The chip thickness can be expressed either by Eq. (13) or (14). Since $h_x=h_y$, the chip thickness can be described by

$$h_{j,\text{stat}}(t) = h_x\sin^2\phi_j(t) + h_y\cos^2\phi_j(t) \tag{21}$$

which holds, since $\sin^2\phi_j(t)+\cos^2\phi_j(t)=1$. Substitution of Eqs. (13) and (14) in Eq. (21) and applying trigonometric relations and subsequently using Eqs. (11) and (4) yields

$$h_{j,\text{stat}}(t) = r - r\cos(\Omega\tau_j(t) - \theta) + \frac{f_z}{\hat{\tau}}\tau_j(t)\sin\phi_j(t) \tag{22}$$

Substitution of Eq. (20) in Eq. (22) and rearranging terms gives an expression for the static chip thickness

$$\begin{aligned} h_{j,\text{stat}}(t) = r - r\cos\left(\frac{\theta f_z\cos\phi_j(t)}{f_z\cos\phi_j(t) + \theta r}\right) \\ + \left(\frac{f_z\theta r}{f_z\cos\phi_j(t) + \theta r}\right)\sin\phi_j(t) \end{aligned} \tag{23}$$

If the time-varying delay is not considered, i.e., $\tau_j(t) := \hat{\tau}$, expression (23) conforms with Eq. (2).

2.3 Entry and Exit Angles. For a full immersion cut, the entry angle is usually defined as $\phi_s=0$ rad and the exit angle as $\phi_e=\pi$ rad. However, the tool enters the cut somewhat earlier (i.e., $\phi_s<0$) and leaves the cut somewhat later (i.e., $\phi_e>\pi$). This can be shown using the definition of the chip thickness in Eq. (13). At the entry and exit angles the chip thickness is zero, which gives

$$h_y = \frac{r\cos\phi_j(t) - r\cos\big(\phi_j(t-\tau_j(t)) + \theta\big)}{\cos\phi_j(t)} = 0 \tag{24}$$

Using Eq. (11) this can also be expressed as

$$\frac{r\cos\phi_j(t) - r\cos(\phi_j(t) - \Omega\tau_j(t) + \theta)}{\cos\phi_j(t)} = 0 \tag{25}$$

This is true if the numerator is zero and the denominator is nonzero. This gives two possible solutions of Eq. (25)

$$-\Omega\tau_j(t) + \theta = 2k\pi \tag{26}$$

$$\phi_j(t) - \Omega\tau_j(t) + \theta = -\phi_j(t) + 2k\pi \tag{27}$$

with $k=0,1,2,\ldots$. Substituting Eq. (20) in Eq. (26) and rearranging terms gives

$$\frac{\theta f_z\cos\phi_j(t)}{f_z\cos\phi_j(t) + \theta r} = 2k\pi \tag{28}$$

This does not lead to angles close to 0 or π radians. Substituting Eq. (20) in Eq. (27) and rearranging terms gives

$$\frac{\theta f_z\cos\phi_j(t)}{f_z\cos\phi_j(t) + \theta r} = -2\phi_j(t) + 2k\pi \tag{29}$$

This equation can not be solved analytically. Therefore, Eq. (29) is approximated using Taylor's series.

For a full immersion cut, the entry angle can be described by $\phi_s=0+\delta\phi_s=\delta\phi_s$, with $|\delta\phi_s| \ll 1$. Applying a Taylor's series expansion, ($\cos\delta\phi_s \approx 1$) to Eq. (29), for $k=0$, the entry angle ϕ_s can be approximated by

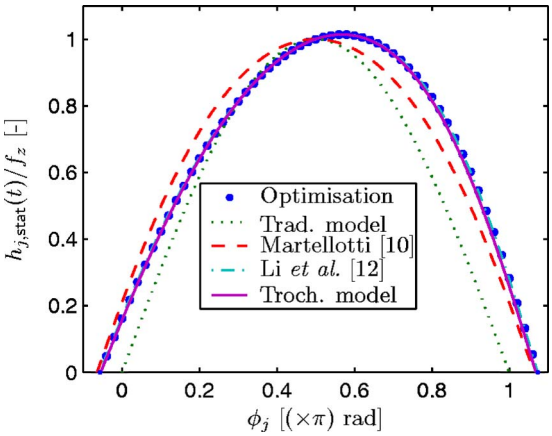

Fig. 5 Chip thickness as a function of rotation angle for various models: r=5 mm, z=2, f_z=2 mm/tooth

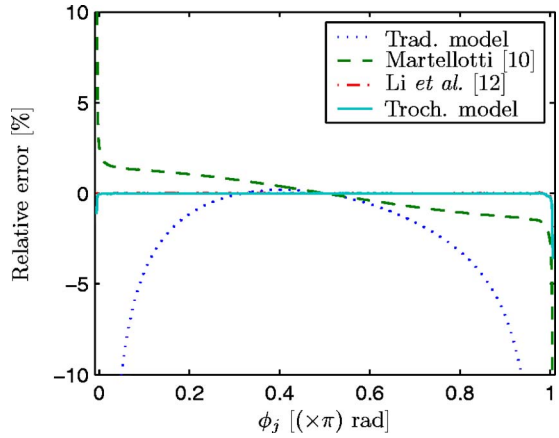

Fig. 6 Relative error in chip thickness as a function of rotation angle for various models: r=5 mm, z=2, f_z=0.2 mm/tooth

$$\phi_s = \delta\phi_s \approx -\frac{\theta f_z}{2(f_z + \theta r)} \tag{30}$$

For a full immersion cut, the exit angle can be described by $\phi_e = \phi_j(t) = \pi + \delta\phi_e$, with $|\delta\phi_e| \ll 1$. Applying Taylor's series, $(\cos(\pi + \delta\phi_e) \approx -1)$ to Eq. (29), for $k=1$, the exit angle ϕ_e can be approximated by

$$\phi_e = \pi + \delta\phi_e \approx \pi - \frac{\theta f_z}{2(f_z - \theta r)} \tag{31}$$

2.4 Results of the Tool Path Model. In the trochoidal model, in contrast with the traditional model Eq. (2), the static chip thickness is described by Eq. (23). The delay, which is traditionally assumed constant, is updated using the periodic function Eq. (20). Finally, the entry and exit angles are described by Eqs. (30) and (31), respectively.

For verification purposes, the approximate model for the chip thickness Eq. (23) is compared to the chip thickness computed numerically using the following optimization scheme. First, the delay is computed numerically by minimizing the absolute value of the left hand side of Eq. (16) via a constrained optimization function with the boundary condition $0.75\hat{\tau} \leqslant \tau_j(t) \leqslant 1.25\hat{\tau}$. This boundary condition is necessary to compute solutions where only the latest tool passing is used. This delay is substituted in Eq. (22) to calculate the chip thickness. The resulting chip thickness is compared to the chip thickness using the circular tooth path of Eq. (2), the trochoidal model of Eq. (23), and the models of Refs. [10,12]. In Ref. [10] the chip thickness is approximated by

$$h_{j,\mathrm{stat}}(t) = r + f_z \sin(\phi_j(t)) - \sqrt{r^2 - f_z^2 \cos^2 \phi_j(t)} \tag{32}$$

In Ref. [12] the chip thickness is approximated by

$$h_{j,\mathrm{stat}}(t) = r\left(1 - \left(1 - \frac{2f_z \sin\phi_j(t)}{r + \frac{zf_z}{2\pi}\cos\phi_j(t)} - \frac{f_z^2 \cos 2\phi_j(t)}{\left(r + \frac{zf_z}{2\pi}\cos\phi_j(t)\right)^2} + \frac{f_z^3 \sin\phi_j(t)\cos^2\phi_j(t)}{\left(r + \frac{zf_z}{2\pi}\cos\phi^j(t)\right)^3}\right)^{1/2}\right) \tag{33}$$

In Fig. 5, the chip thickness is shown for r=5 mm and z=2 and a rather unrealistic chip load f_z=2 mm/tooth. This value is chosen to magnify the differences between the various models for visualization purposes. The trochoidal model of Eq. (23) and the model of Ref. [12] fit the numerical results very well. It can be seen that the chip thickness function does not have a symmetry axis at $\phi = 0.5\pi$. However, the model of Ref. [10] and the traditional model do have this symmetry axis. Furthermore, the maximum chip thickness is larger than the chip load f_z according to the numerical results. This is also predicted by the model of Ref. [12] and the proposed trochoidal model of Eq. (23), whereas the traditional and the model in Ref. [10] do not predict this.

The errors of the chip thickness of the various models relative to the numerically computed chip thickness are shown in Fig. 6. Here a more realistic case of f_z=0.2 mm/tooth is taken. Herein, the differences between the models are clearly visible. Especially when the chip thickness is small, the relative error becomes very large for both the traditional model and the model of Ref. [10]. For the trochoidal model of Eq. (23) and the model of Ref. [12], the errors are rather small. The drawback of the model in Ref. [12] is that is does not give an expression for the delay.

The entry and exit angles according to Eqs. (30) and (31) are shown in Fig. 7 for the case where f_z=0.2 mm/tooth. The results of the various models, shown in Fig. 5, are also presented in this figure. The expressions that are found for the entry and exit angles match very well with the angles where the chip thickness of the trochoidal model is zero.

The delay expressed by Eq. (20) is compared to the delay calculated numerically using the optimization function. The results can be seen in Fig. 8. In this figure, only half the period is shown, since during the other half, the cutter is not in cut. Results of the proposed model fit the numerical results very well. For small angles, the delay is smaller than the constant delay $\hat{\tau}$. This corresponds to the situation shown in Fig. 3 where point O is the point at $t - \hat{\tau}$ and point N the point at $t - \tau_2$. When cutting, the tooth reaches point O sooner than point N and hence $\tau_j(t) < \hat{\tau}$. If $0.5\pi < \phi_j(t) < \phi_e$, the delay becomes larger than $\hat{\tau}$. Then point O' is reached later than point N', where the prime symbolizes the new

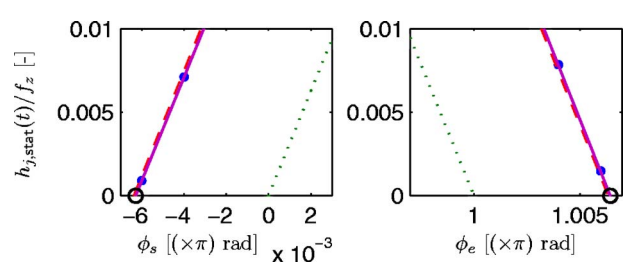

Fig. 7 Entry (left) and exit (right) angles. The values from Eqs. (30) and (31) are plotted as circles; r=5 mm, z=2, f_z=0.2 mm/tooth. For legend, see Fig. 5.

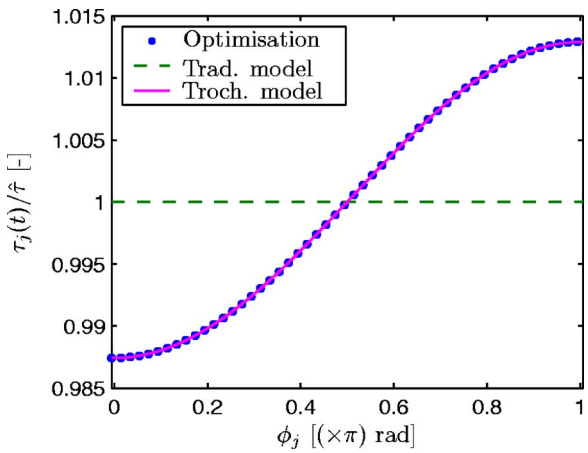

Fig. 8 Normalized delay as a function of rotation angle: r =5 mm, z=2, f_z=0.2 mm/tooth

position of points O and N.

The relative error of both the time delay and chip thickness of the traditional model increases as the chip thickness becomes smaller. Since the chip thickness is very small in low immersion cutting, it is likely that the use of the traditional model leads to errors for this type of cut. Therefore, in Sec. 4, the stability of milling models using both tooth path models is investigated. In the next section, the total milling model is presented in more detail.

2.5 The Milling System. The milling model represented by Fig. 2, contains several blocks. First, the block Machine will be presented in more detail. The dynamics of the machine (due to flexibilities of the tool, toolholder, and spindle system) are represented as a 2 degree of freedom (2DOF) mass–spring–damper system in Fig. 1. For representing general linear dynamics, a state-space formulation is used

$$\dot{\underline{z}}(t) = \mathbf{A}\underline{z}(t) + \mathbf{B}\underline{u}(t)$$

$$\underline{y}(t) = \mathbf{C}\underline{z}(t) + \mathbf{D}\underline{u}(t) \tag{34}$$

These equations describe the relation between the input $\underline{u}$ of a system (in our case the force that acts on the mill, i.e. $\underline{u}(t)=\underline{F}(t)$) and the output $\underline{y}$ of this system (in our case the displacement of the tip of the mill, i.e. $\underline{y}(t)=\underline{v}(t)$).

Since in the milling equations both the x and y directions are necessary (assuming these dynamics are uncoupled), the state vectors of these two directions, $\underline{z}_x$ and $\underline{z}_y$, are assembled in a single state vector $\underline{z}(t)=[\underline{z}_x^T(t)\ \underline{z}_y^T(t)]^T$, which yields the following set of differential equations describing the machine dynamics

$$\dot{\underline{z}}(t) = \begin{bmatrix} \dot{\underline{z}}_x(t) \\ \dot{\underline{z}}_y(t) \end{bmatrix} = \begin{bmatrix} \mathbf{A}_x & \mathbf{0} \\ \mathbf{0} & \mathbf{A}_y \end{bmatrix} \begin{bmatrix} \underline{z}_x(t) \\ \underline{z}_y(t) \end{bmatrix} + \begin{bmatrix} \mathbf{B}_x & \mathbf{0} \\ \mathbf{0} & \mathbf{B}_y \end{bmatrix} \begin{bmatrix} u_x(t) \\ u_y(t) \end{bmatrix} = \mathbf{A}\underline{z}(t) + \mathbf{B}\underline{u}(t)$$

$$\underline{y}(t) = \begin{bmatrix} y_x(t) \\ y_y(t) \end{bmatrix} = \begin{bmatrix} \mathbf{C}_x & \mathbf{0} \\ \mathbf{0} & \mathbf{C}_y \end{bmatrix} \begin{bmatrix} \underline{z}_x(t) \\ \underline{z}_y(t) \end{bmatrix} + \begin{bmatrix} \mathbf{D}_x & \mathbf{0} \\ \mathbf{0} & \mathbf{D}_y \end{bmatrix} \begin{bmatrix} u_x(t) \\ u_y(t) \end{bmatrix} = \mathbf{C}\underline{z}(t) + \mathbf{D}\underline{u}(t) \tag{35}$$

When the dynamics are modeled as a 2DOF linear mass–spring–damper system, as depicted in Fig. 1, the state $\underline{z}_i$ can be defined by $\underline{z}_i=[v_i\ \dot{v}_i]^T$. This yields

$$\mathbf{A}_i = \begin{bmatrix} 0 & 1 \\ -\dfrac{k_i}{m_i} & -\dfrac{b_i}{m_i} \end{bmatrix}, \quad \mathbf{B}_i = \begin{bmatrix} 0 \\ \dfrac{1}{m_i} \end{bmatrix}^T$$

$\mathbf{C}_i=[1000\ 0]$, and $\mathbf{D}_i=0$, where $i=x,y$ and m_i, b_i, and k_i represent the mass, damping, and stiffness coefficients, respectively. However, more complex linear dynamics can be modeled using the state-space representation of Eq. (35).

The new tooth path model has consequences for the blocks Cutting and Delay in Fig. 2. The force that acts on the tooth j in tangential and radial directions can be described by a so-called exponential cutting force model [8,18]

$$F_{t_j}(t) = K_t a_p h_j(t)^{x_F} g_j(\phi_j(t))$$

$$F_{r_j}(t) = K_r a_p h_j(t)^{x_F} g_j(\phi_j(t)) \tag{36}$$

where $0<x_F\leqslant 1$, and $K_t,K_r>0$ are cutting parameters. The function $g_j(\phi_j(t))$ describes whether a tooth is in or out of cut

$$g_j(\phi_j(t)) = \begin{cases} 1, & \phi_s \leqslant \phi_j(t) \leqslant \phi_e \wedge h_j(t) > 0 \\ 0, & \text{else} \end{cases} \tag{37}$$

This exponential model has the benefit that the stability lobes are dependent on the feed rate. In Ref. [18], it was found that this dependency occurs in practice. However, a drawback of this model is the fact that it is nonsmooth for $h=0$. Moreover, in order to compute the stability limit, it is necessary to calculate $\partial F_{t_j,r_j}/\partial h_j$, which is singular for $h_j=0$. Therefore, it is multiplied by a window function

$$\exp\left(\frac{-10^{-4}}{h_j(t)}\right)$$

Note that for $h_j(t)<0$, the forces are still zero due to the fact that in that case $g_j(\phi_j(t))=0$, see Eq. (37). Resuming, the force model can be formulated as

$$F_{t_j}(t) = \exp\left(\frac{-10^{-4}}{h_j(t)}\right) K_t a_p h_j(t)^{x_F} g_j(\phi_j(t))$$

$$F_{r_j}(t) = \exp\left(\frac{-10^{-4}}{h_j(t)}\right) K_r a_p h_j(t)^{x_F} g_j(\phi_j(t)) \tag{38}$$

Using this window function, overcomes the problem of the singularity of $\partial F_{t_j,r_j}/\partial h_j$. Moreover, if this window function is used, the cutting force is a continuously differentiable function of the chip thickness. The factor -10^{-4} in this smooth window function is empirically determined such that the difference between Eqs. (36) and (38) is less than 1% for $h_j\geqslant 0.01$ mm. On the other hand, when the factor would be chosen even smaller, the singularity $\lim_{h_j\downarrow 0} \partial F_{t_j,r_j}/\partial h_j$ of the nonsmooth function would become dominant in the calculation of the stability.

After substitution of Eqs. (1), (3), and (37), and summing for all teeth, Eq. (38) can be described in feed x and normal y direction as

$$\underline{F}(t) = a_p \sum_{j=0}^{z-1} g_j(\phi_j(t)) \exp\left(\frac{-10^{-4}}{h_j(t)}\right) h_j(t)^{x_F} \mathbf{S}(t) \begin{bmatrix} K_t \\ K_r \end{bmatrix} \tag{39}$$

with

$$h_j(t) = h_{j,\text{stat}}(t) + [\sin\phi_j(t)\ \cos\phi_j(t)]\big(\underline{v}(t) - \underline{v}(t-\tau_j(t))\big) \tag{40}$$

and $\underline{F}(t)=[F_x(t)\ F_y(t)]^T$, and $F_x(t)$ and $F_y(t)$ the forces in x and y directions, respectively. Furthermore, $\underline{v}(t)=[v_x(t)\ v_y(t)]^T$, and

$$\mathbf{S}(t) = \begin{bmatrix} -\cos\phi_j(t) & -\sin\phi_j(t) \\ \sin\phi_j(t) & -\cos\phi_j(t) \end{bmatrix}$$

Substitution of Eq. (39) as input $\underline{u}$ into Eq. (35) and realizing that $\underline{v}(t)=\underline{y}(t)=\mathbf{C}\underline{z}(t)$ (assuming that $\mathbf{D}=\mathbf{0}$) gives

$$\dot{\underline{z}}(t) = \mathbf{A}\underline{z}(t) + \mathbf{B}a_p\sum_{j=0}^{z-1} g_j(\phi_j(t))\exp\left(\frac{-10^{-4}}{h_j(t)}\right)h_j(t)^{x_F}\mathbf{S}(t)\begin{bmatrix}K_t\\K_r\end{bmatrix}$$

$$\underline{y}(t) = \mathbf{C}\underline{z}(t) \tag{41}$$

with

$$h_j(t) = h_{j,\text{stat}}(t) + [\sin\phi_j(t)\ \cos\phi_j(t)]\mathbf{C}\big(\underline{z}(t) - \underline{z}(t-\tau_j(t))\big) \tag{42}$$

It is assumed that this system has a periodic solution with period time $T=\hat{\tau}$. In Sec. 3, a method is presented to numerically find this periodic solution using the finite difference method. The existence of this periodic solution is not proven here, but for the considered parameters in this paper, the periodic solution has always been found. Let us now assume that the periodic solution is known and denote it by $\underline{z}^*(t)$. If chatter occurs, this periodic solution is unstable and otherwise it is stable. In order to determine the (local) stability properties of $\underline{z}^*(t)$, Eq. (41) is linearized about the periodic solution $\underline{z}^*(t)$. Using the decomposition $\underline{z}(t)=\underline{z}^*(t)+\underline{\tilde{z}}(t)$, such linearization yields the following linearized dynamics

$$\begin{aligned}\dot{\underline{\tilde{z}}}(t) = \mathbf{A}\underline{\tilde{z}} + \mathbf{B}a_p\sum_{j=0}^{z-1} g_j(\phi_j(t))\Bigg(&x_F h_j^*(t)^{x_F-1}\exp\left(\frac{-10^{-4}}{h_j^*(t)}\right)\\ &+ h_j^*(t)^{x_F}\exp\left(\frac{-10^{-4}}{h_j^*(t)}\right)\frac{10^{-4}}{h_j^*(t)^2}\Bigg)\mathbf{S}(t)\begin{bmatrix}K_t\\K_r\end{bmatrix}\\ &\times[\sin\phi_j(t)\ \cos\phi_j(t)]\mathbf{C}\big(\underline{\tilde{z}}(t) - \underline{\tilde{z}}(t-\tau_j(t))\big)\end{aligned}$$

$$\underline{\tilde{y}}(t) = \mathbf{C}\underline{\tilde{z}}(t) \tag{43}$$

with

$$h_j^*(t) = h_{j,\text{stat}}(t) + [\sin\phi_j(t)\ \cos\phi_j(t)]\mathbf{C}\big(\underline{z}^*(t) - \underline{z}^*(t-\tau_j(t))\big) \tag{44}$$

Equation (43) can be abbreviated by

$$\dot{\underline{\tilde{z}}}(t) = \mathbf{A}\underline{\tilde{z}} + \mathbf{B}a_p\sum_{j=0}^{z-1}\mathbf{H}_j(t)\mathbf{C}\big(\underline{\tilde{z}}(t) - \underline{\tilde{z}}(t-\tau_j(t))\big)$$

$$\underline{\tilde{y}}(t) = \mathbf{C}\underline{\tilde{z}}(t) \tag{45}$$

with

$$\begin{aligned}\mathbf{H}_j(t) = g_j(\phi_j(t))\Bigg(&x_F h_j^*(t)^{x_F-1}\exp\left(\frac{-10^{-4}}{h_j^*(t)}\right)\\ &+ h_j^*(t)^{x_F}\exp\left(\frac{-10^{-4}}{h_j^*(t)}\right)\frac{10^{-4}}{h_j^*(t)^2}\Bigg)\mathbf{S}(t)\begin{bmatrix}K_t\\K_r\end{bmatrix}\\ &\times[\sin\phi_j(t)\ \cos\phi_j(t)]\end{aligned} \tag{46}$$

The semi-discretization method of Refs. [16,19] can be used to determine the stability properties of delayed linear periodic time-varying systems of the form

$$\dot{\underline{z}}(t) = \mathbf{P}(t)\underline{z}(t) + \sum_{j=0}^{z-1}\mathbf{Q}_j^*(t)\underline{z}(t-\tau_j(t))$$

$$\mathbf{P}(t+T) = \mathbf{P}(t), \quad \mathbf{Q}_j^*(t+T) = \mathbf{Q}_j^*(t) \tag{47}$$

with T the period time of the matrices $\mathbf{P}(t)$ and $\mathbf{Q}_j^*(t)$. Since the state $\underline{z}$ may be quite large for high-order machine dynamics, it is more convenient to slightly adjust this equation to

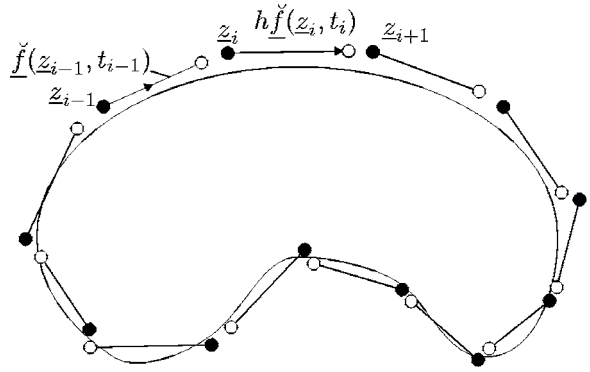

Fig. 9 Graphical interpretation of the finite difference method for ODEs

$$\dot{\underline{z}}(t) = \mathbf{P}(t)\underline{z}(t) + \sum_{j=0}^{z-1}\mathbf{Q}_j(t)\underline{y}(t-\tau_j(t))$$

$$\mathbf{P}(t+T) = \mathbf{P}(t), \quad \mathbf{Q}_j(t+T) = \mathbf{Q}_j(t) \tag{48}$$

where $\mathbf{Q}_j^*(t)=\mathbf{Q}_j(t)\mathbf{C}$, $j=0,\ldots,z-1$. The first equation in Eq. (45) is written in the form of Eq. (48) with

$$\mathbf{P}(t) = \mathbf{A} + a_p\sum_{j=0}^{z-1}\mathbf{B}\mathbf{H}_j(t)\mathbf{C} \tag{49}$$

$$\mathbf{Q}_j(t) = -a_p\mathbf{B}\mathbf{H}_j(t), \quad j=0,\ldots,z-1 \tag{50}$$

Since

$$\begin{aligned}&\mathbf{H}_j(t+\hat{\tau})\mathbf{C}\underline{z}(t+\hat{\tau}-\tau_j(t+\hat{\tau}))\\ &\quad = \mathbf{H}_{j-1}(t)\mathbf{C}\underline{z}(t-\tau_{j-1}(t)), \quad j=0,\ldots,z-1\end{aligned} \tag{51}$$

Eq. (45) is periodic with period time $\hat{\tau}$.

The choice whether the tool path is modeled as a circular arc or as a trochoid influences the delay, which is constant for the circular tool path and periodic for the trochoid tool path. Furthermore, the matrix $\mathbf{H}_j(t)$ changes as a result of the different entry and/or exit angles (see Eqs. (30) and (31)) and the new formulation for the static chip thickness. However, the structure of the model as presented in Eq. (48) does not change. Therefore, the semi-discretization method can be used for both models. This will be shown in Sec. 4. First, the method to find the periodic solution $\underline{z}^*(t)$ is presented in the next section.

3 Periodic Solutions

In this section, a periodic solution $\underline{z}(t+T)=\underline{z}(t)$ with period time T of the DDE

$$\dot{\underline{z}}(t) = \underline{f}\big(\underline{z}(t), \underline{z}(t-\tau(t)), t\big), \quad \tau(t+T) = \tau(t) \tag{52}$$

is approximated using the finite difference method (FDM). This method (see e.g., Refs. [22,23]) is a well-known method to approximate periodic solutions of an ordinary differential equation (ODE) of the form

$$\dot{\underline{z}}(t) = \underline{\breve{f}}(\underline{z}(t), t), \quad \underline{z}(t+T) = \underline{z}(t) \tag{53}$$

by a number of segments (see Fig. 9).

The method uses a sequence of N points $\underline{Z}=[\underline{z}_1^T\ldots\underline{z}_i^T\ldots\underline{z}_N^T]^T$, on a time grid with step length h. Here, the method is described for an equidistant grid with step length $h=T/N$, but it can easily be modified for a nonequidistant grid. Since in the case of a milling model, one has to deal with a periodic DDE with known period time T, in this section it is also assumed that the DDE Eq. (52) is periodic and the period time is known. This makes the method

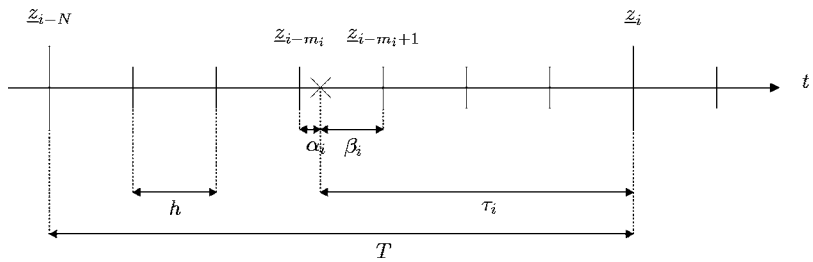

Fig. 10 Graphical interpretation of period time and the delay. In this case $\tau_i \neq m_i h$.

easier, since no anchor equation is necessary in order to approximate the period time. The delayed state $\underline{z}(t-\tau(t))$ is approximated by linear interpolation between the two closest discretization points (see Fig. 10). Then

$$\underline{z}(t_i) = \underline{z}_i \tag{54}$$

$$\underline{z}(t_i - \tau(t_i)) \approx a_i \underline{z}_{i-m_i+1} + b_i \underline{z}_{i-m_i} \tag{55}$$

with $a_i = \alpha_i/(\alpha_i+\beta_i)$, $b_i = \beta_i/(\alpha_i+\beta_i)$, $\alpha_i+\beta_i = h$, and $m_i = \lceil \tau(t_i)/h \rceil$.

In Fig. 9, the forward Euler scheme is shown for an ODE, i.e., $\underline{z}_{i+1} = \underline{z}_i + h\underline{\breve{f}}(\underline{z}_i, t_i)$. However, other schemes can also be used, like the trapezoidal scheme, which can be described for ODEs as

$$\underline{z}_{i+1} = \underline{z}_i + \frac{h}{2}(\underline{\breve{f}}(\underline{z}_i, t_i) + \underline{\breve{f}}(\underline{z}_{i+1}, t_{i+1})) \tag{56}$$

Using this latter scheme, Eq. (52) can be approximated by

$$\underline{z}_{i+1} = \underline{z}_i + \frac{h}{2}(\underline{f}(\underline{z}_i, a_i \underline{z}_{i-m+1} + b_i \underline{z}_{i-m}, t_i) + \underline{f}(\underline{z}_{i+1}, a_{i+1}\underline{z}_{i-m+2} + b_{i+1}\underline{z}_{i-m+1}, t_{i+1})) \tag{57}$$

The finite difference method is based on finding a zero of the function

$$\underline{H} = \begin{bmatrix} \underline{z}_1 - \underline{z}_2 + \frac{h}{2}(\underline{f}(\underline{z}_1, a_1\underline{z}_{2-m} + b_1\underline{z}_{1-m}, t_1) + \underline{f}(\underline{z}_2, a_2\underline{z}_{3-m} + b_2\underline{z}_{2-m}, t_2)) \\ \vdots \\ \underline{z}_i - \underline{z}_{i+1} + \frac{h}{2}(\underline{f}(\underline{z}_i, a_i\underline{z}_{i-m+1} + b_i\underline{z}_{i-m}, t_i) + \underline{f}(\underline{z}_{i+1}, a_{i+1}\underline{z}_{i-m+2} + b_{i+1}\underline{z}_{i-m+1}, t_{i+1})) \\ \vdots \\ \underline{z}_N - \underline{z}_{N+1} + \frac{h}{2}(\underline{f}(\underline{z}_N, a_N\underline{z}_{N-m+1} + b_N\underline{z}_{N-m}, t_N) + \underline{f}(\underline{z}_{N+1}, a_{N+1}\underline{z}_{N-m+2} + b_{N+1}\underline{z}_{N-m+1}, t_{N+1})) \end{bmatrix} \tag{58}$$

Since $\underline{z}(T+t) = \underline{z}(t)$, it follows that $\underline{z}_{N+i} = \underline{z}_i$. A zero of Eq. (58) can be found by applying the Newton–Raphson algorithm; i.e., we solve iteratively the set of equations

$$\frac{\partial \underline{H}}{\partial \underline{Z}} \Delta \underline{Z} = -\underline{H}(\underline{Z}) \tag{59}$$

Each row in Eq. (58) has the same pattern which can be simplified to

$$\underline{g}_i = \underline{p}_{i1} - \underline{p}_{i2} + \frac{h}{2}(\underline{f}(\underline{p}_{i1}, a_i\underline{q}_{i1} + b_i\underline{q}_{i2}, t_i) + \underline{f}(\underline{p}_{i2}, a_{i+1}\underline{q}_{i3} + b_{i+1}\underline{q}_{i1}, t_{i+1})), \quad i = 1, \ldots, N \tag{60}$$

where $\underline{p}_{i1} = \underline{z}_i$, $\underline{p}_{i2} = \underline{z}_{i+1}$, $\underline{q}_{i1} = \underline{z}_{i-m+1}$, $\underline{q}_{i2} = \underline{z}_{i-m}$, and $\underline{q}_{i3} = \underline{z}_{i-m+2}$. Therefore, the partial derivative of $\underline{g}_i$ should be calculated with respect to five terms, namely $\underline{p}_{i1}$, $\underline{p}_{i2}$, $\underline{q}_{i1}$, $\underline{q}_{i2}$, and $\underline{q}_{i3}$.

This gives

$$\frac{\partial \underline{H}}{\partial \underline{Z}} = \begin{bmatrix} \mathbf{a}_{11} & \mathbf{a}_{12} & 0 & \ldots & 0 & 0 \\ 0 & \mathbf{a}_{22} & \mathbf{a}_{23} & \ldots & 0 & 0 \\ \ddots & \ddots & \ddots & \ddots & \ddots & \ddots \\ 0 & 0 & 0 & \ldots & \mathbf{a}_{N-1,N-1} & \mathbf{a}_{N-1,N} \\ \mathbf{a}_{N,1} & 0 & 0 & \ldots & 0 & \mathbf{a}_{NN} \end{bmatrix} + \begin{bmatrix} 0 & \ldots & 0 & \bar{\mathbf{a}}_{1,1-m} & \bar{\mathbf{a}}_{1,2-m} & \bar{\mathbf{a}}_{1,3-m} & 0 & \ldots & 0 \\ 0 & \ldots & 0 & 0 & \bar{\mathbf{a}}_{2,2-m} & \bar{\mathbf{a}}_{2,3-m} & \bar{\mathbf{a}}_{2,4-m} & \ldots & 0 \\ \ddots & \ddots & \ddots & \ddots & \ddots & \ddots & \ddots & \ddots & \ddots \\ 0 & \ldots & \bar{\mathbf{a}}_{N,N-m} & \bar{\mathbf{a}}_{N,N-m+1} & \bar{\mathbf{a}}_{N,N-m+2} & 0 & 0 & \ldots & 0 \end{bmatrix} \tag{61}$$

with

$$\mathbf{a}_{i,i} = \mathbf{I} + \frac{h}{2}\frac{\partial \underline{f}(\underline{p}_{i1}, a_i\underline{q}_{i1} + b_i\underline{q}_{i2}, t_i)}{\partial \underline{p}_{i1}}$$

$$\mathbf{a}_{i,i+1} = -\mathbf{I} + \frac{h}{2}\frac{\partial \underline{f}(\underline{p}_{i2}, a_{i+1}\underline{q}_{i3} + b_{i+1}\underline{q}_{i1}, t_{i+1})}{\partial \underline{p}_{i2}}$$

$$\bar{\mathbf{a}}_{i,i-m} = \frac{h}{2}\frac{\partial \underline{f}(\underline{p}_{i1}, a_i\underline{q}_{i1} + b_i\underline{q}_{i2}, t_i)}{\partial \underline{q}_{i2}}$$

$$\bar{\mathbf{a}}_{i,i-m+1} = \frac{h}{2}\frac{\partial \underline{f}(\underline{p}_{i1}, a_i\underline{q}_{i1} + b_i\underline{q}_{i2}, t_i)}{\partial \underline{q}_{i1}} + \frac{h}{2}\frac{\partial \underline{f}(\underline{p}_{i2}, a_{i+1}\underline{q}_{i3} + b_{i+1}\underline{q}_{i1}, t_{i+1})}{\partial \underline{q}_{i1}}$$

$$\bar{\mathbf{a}}_{i,i-m+2} = \frac{h}{2}\frac{\partial \underline{f}(\underline{p}_{i2}, a_{i+1}\underline{q}_{i3} + b_{i+1}\underline{q}_{i1}, t_{i+1})}{\partial \underline{q}_{i3}} \tag{62}$$

Here, the equations in Eq. (62), respectively, conform with $\partial \underline{g}_i/\partial \underline{p}_{i1}$, $\partial \underline{g}_i/\partial \underline{p}_{i2}$, $\partial \underline{g}_i/\partial \underline{q}_{i2}$, $\partial \underline{g}_i/\partial \underline{q}_{i1}$, and $\partial \underline{g}_i/\partial \underline{q}_{i3}$. The first matrix of Eq. (61) defines the derivation of $\underline{H}$ with respect to the present state and the second matrix defines the derivation of $\underline{H}$ with respect to the delayed state. For systems with multiple delays, this latter matrix needs to be built and added for every delay.

The reason for the notation of $\bar{\mathbf{a}}$ in contrast to $\mathbf{a}$ is the following. The matrix $\partial \underline{H}/\partial \underline{Z}$ is of size $N \times N$. However, it can occur that terms such as $\bar{\mathbf{a}}_{i,i-m}$ fall outside this matrix if $i-m<0$ or $i-m>N$. In that case, the term changes to $\bar{\mathbf{a}}_{i,i-m+\gamma N}$, where γ is chosen such that $0<i-m+\gamma N \leqslant N$. This can be done, due to the periodicity of the system and the periodicity of the solution.

Using the above scheme for the milling model Eq. (41), the periodic solution $z^*(t)$ is found. Here, an nonequidistant grid is chosen such that just before and just after the tool enters the cut, a grid point exists. The dynamics of the spindle are modeled, in both x and y directions, as a single degree-of-freedom linear mass–spring–damper system, as shown in Fig. 1(b), with masses m_x, m_y, stiffness coefficients k_x, k_y, and damping coefficients b_x, b_y. The natural frequencies of the system are defined by $\omega_x = \sqrt{k_x/m_x}$, $\omega_y = \sqrt{k_y/m_y}$ and the dimensionless damping constants by $\zeta_x = b_x/2\sqrt{m_x k_x}$, $\zeta_y = b_y/2\sqrt{m_y k_y}$. The parameters used in the model are $m_x = m_y = 0.02$ kg, $\zeta_x = \zeta_y = 0.05$, $\omega_x = \omega_y = 2\pi \cdot 2198$ rad/s, $K_t = 462$ N/mm$^{1+x_F}$, $K_r = 38.6$ N/mm$^{1+x_F}$, $x_F = 0.744$, $r = 5$ mm, $f_z = 0.2$ mm/tooth, $a_e = 10$ mm (=100% immersion), $\Omega = 30{,}000$ rpm, $z = 2$, and $N = 600$. The cutting parameters K_t, K_r, and x_F are adopted from Ref. [18]. The results are shown in Fig. 11. In this figure, the results for the finite difference method are combined with the results from time simulation over 20 revolutions where $\underline{z}(t<0) = \underline{0}$. In Fig. 11($a$), the depth of cut is chosen such that no chatter occurs, whereas in Fig. 11(b), the depth of cut is increased in order to have chatter. As can be seen, even if chatter occurs, the (unstable) periodic solution still can be found by the finite difference method. Also for lower values of N, the periodic solution is found, but of course the shape is more coarse than the one displayed in Fig. 11. For the simulations in time domain, model (41) is used, which is nonlinear in $\underline{v}$. Therefore, when chatter occurs, the tool leaves the cut due to the large vibrations and the tool displacement remains bounded.

The stability of the periodic solution can be evaluated using the semi-discretization method. This is shown in the next section.

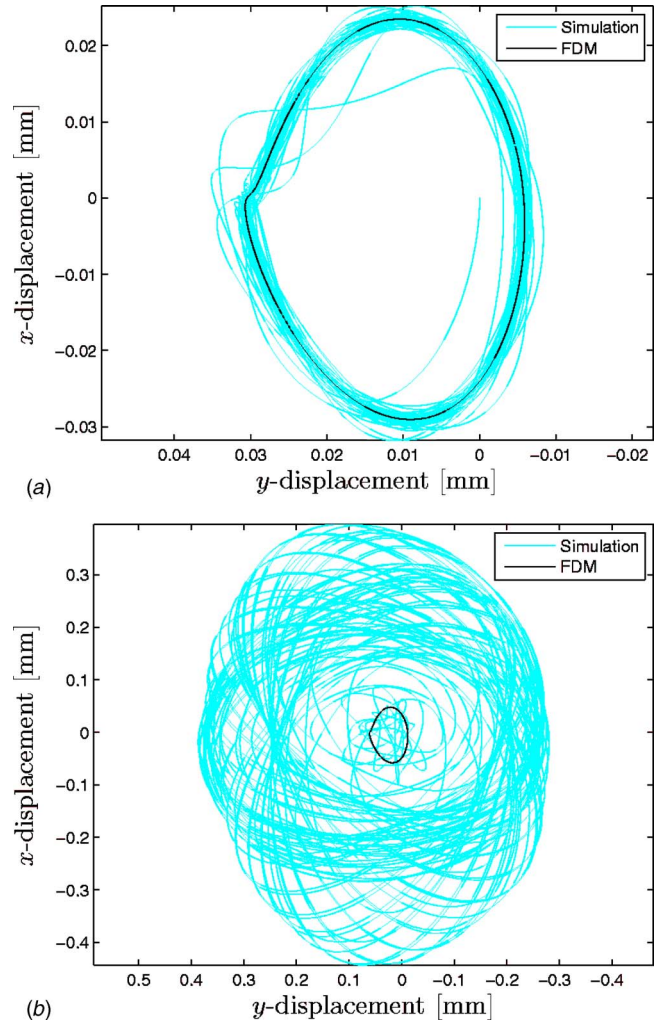

Fig. 11 Displacement of the tool. Periodic solution using the finite difference method and numerical simulation of 20 revolutions (axis directions as in Fig. 3). (a) a_p=1 mm; stable cut. (b) a_p=2 mm; unstable cut.

4 Stability

In Ref. [16], the semi-discretization method is demonstrated for a nonautonomous system with a constant delay. In Ref. [19], the method was demonstrated for an autonomous system with a periodic delay, where this periodic delay was due to a periodically varying spindle speed. The milling model presented in Sec. 2 is a nonautonomous system with multiple periodic delays (which are due to the trochoidal nature of the toolpath). Using the semi-discretization method for this model is straightforward by combining the two cases discussed in Refs. [16,19].

Whenever a mill is cutting, the tool experiences a displacement. This displacement is periodic with the tooth passing time $T = \hat{\tau}$ and is a result of the forces acting on the tool while cutting. In the model, this displacement is a periodic solution of Eq. (41). When no chatter occurs this periodic solution is stable and when chatter occurs it is unstable. Therefore, the chatter boundary can be found by regarding the stability of this periodic solution, which is assessed by considering the eigenvalues of the monodromy matrix.

This matrix describes the transformation from a state of the linearized system at $t_0 = 0$ to the state at $t = T$, where T is the period time of the periodic solution. If all the eigenvalues of the monodromy matrix, which are called the Floquet multipliers, are in modulus less than one, the periodic solution is stable. If one or more of the eigenvalues lie outside the unit circle, the periodic solution is unstable. The semi-discretization method gives a finite-dimensional approximation of the monodromy matrix Φ of a periodic DDE over the principal period T. The period T is divided

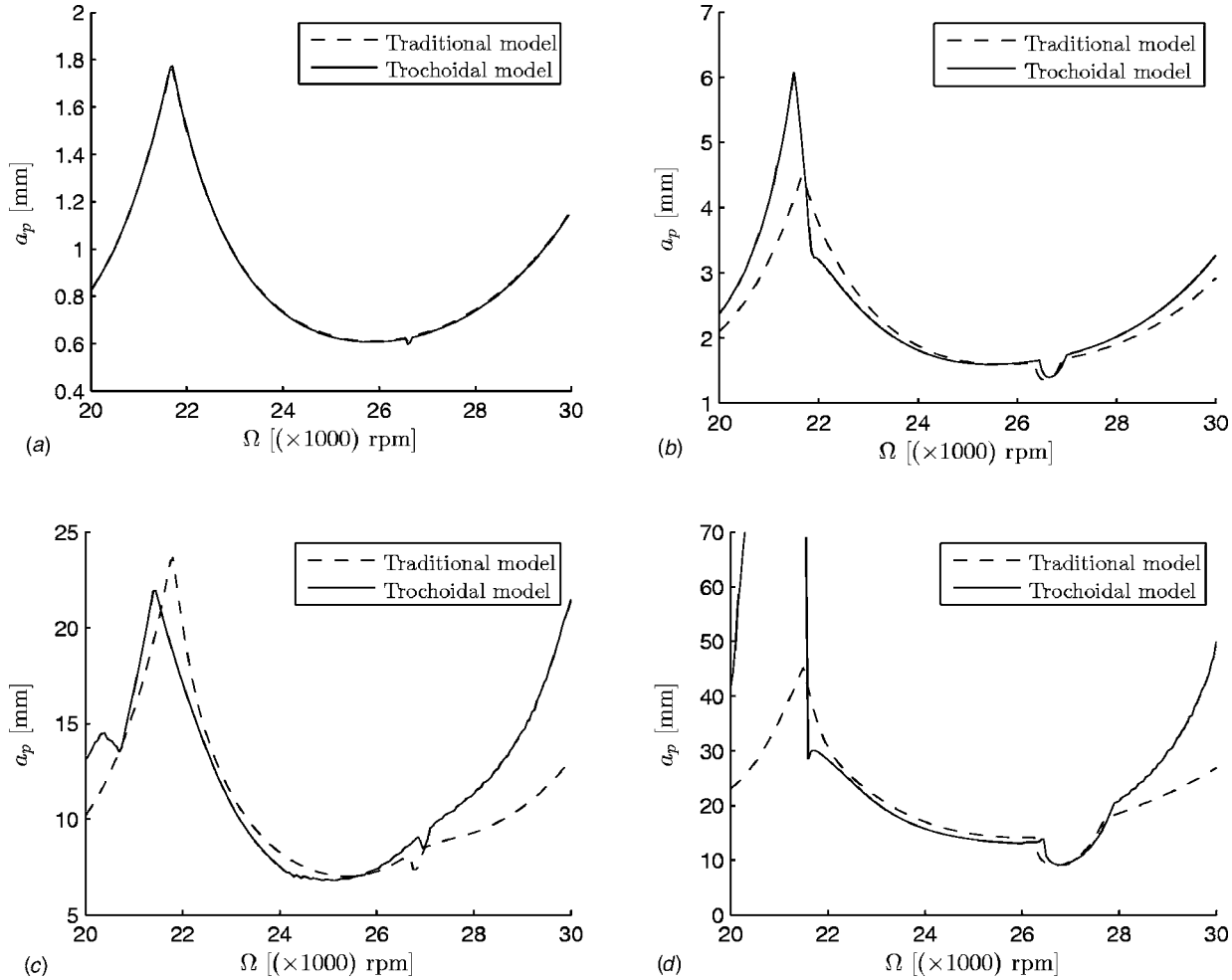

Fig. 12 Stability lobes for upmilling using the traditional and the trochoidal model for several immersion levels. (*a*) 100% immersion; (*b*) 50% immersion; (*c*) 10% immersion; (*d*) 5% immersion.

into k intervals of length Δt. Here, the method is described for an equidistant grid, but it can easily be converted to a nonequidistant grid. A vector $\underline{q}_i$ is built containing the present and the delayed states $\underline{q}_i=[\underline{z}_i^T\ \underline{z}_{i-1}^T \ldots \underline{z}_{i-M}^T]^T$, $i=0,\ldots,k$, and $M=[\max \tau(t)/h]$. The method computes the matrix $\mathbf{\Gamma}_i$ such that $\underline{q}_{i+1}=\mathbf{\Gamma}_i\underline{q}_i$. The monodromy matrix can now simply be computed by $\mathbf{\Phi}=\mathbf{\Gamma}_k\mathbf{\Gamma}_{k-1}\ldots\mathbf{\Gamma}_1$. If the dimension of the state is large compared to the number of outputs, it is computationally more beneficial to include the present state and the delayed outputs in the vector $\underline{q}_i$, i.e., $\underline{q}_i=[\underline{z}_i^T\ \underline{y}_{i-1}^T \ldots \underline{y}_{i-M}^T]^T$. This adjustment is also described by Eq. (48).

Stability lobes have been generated using the traditional tool path model and the model presented in Sec. 2. At each combination of spindle speed and depth of cut, first the periodic solution is computed using the finite difference method. Next, the stability of the periodic solution is assessed using the semi-discretization method. The parameter k is chosen to be 60. Here, also a nonequidistant grid is chosen such that just before and just after the tool enters the cut, a grid point exists. The same parameters have been used as mentioned in Sec. 3.

The stability lobes for up- and downmilling are shown in Figs. 12 and 13, respectively. In these figures, a wide range of immersion ratios is chosen in order to analyze the effects on the stability for both full immersion and extreme low immersion milling.

From these figures, it can be concluded that the differences between the stability lobes of both models increase if the radial immersion decreases. The differences in the static chip thickness, entry, and exit angles and delay, as shown in Figs. 6, 7, and 8, respectively, are the largest when the angle is close to 0 or π radians. Therefore, for a low immersion cut these errors have a relatively large effect on the stability.

In Ref. [24], the lobes have been computed using the new tooth path model in combination with a linear cutting force model. In that case, only the shift of the lobes to the left and right can be seen. The extra peak as depicted in Fig. 13(*d*) does not occur in that case.

A further discussion on the resulting stability lobes is presented in the next section.

5 Discussion

The differences between the stability lobes using the traditional model and the trochoidal model are mainly due to the periodic motion of the cutter. For downmilling, on the right side of the peak an increase in the stability limit can be seen, which results even in an extra peak for 5% downmilling. For upmilling, the same effect can be seen on the left side of the peak. Here, an extra peak occurs for 10% immersion and for 50% and 5% immersion, the stability limit increases drastically near the peak of the lobe. Due to the periodic motion of the cutter, it may happen that the cutter loses contact from the workpiece when $\phi_s < \phi_j(t) < \phi_e$ even if no chatter occurs. This is depicted in Fig. 14, where the chip thickness including the periodic vibrations is shown for a cut at 23,650 rpm and $a_p=33$ mm for 5% downmilling, which is just below the top of the second peak in Fig. 13(*d*). This kind of loss of contact has an effect similar to a decrease of radial immersion

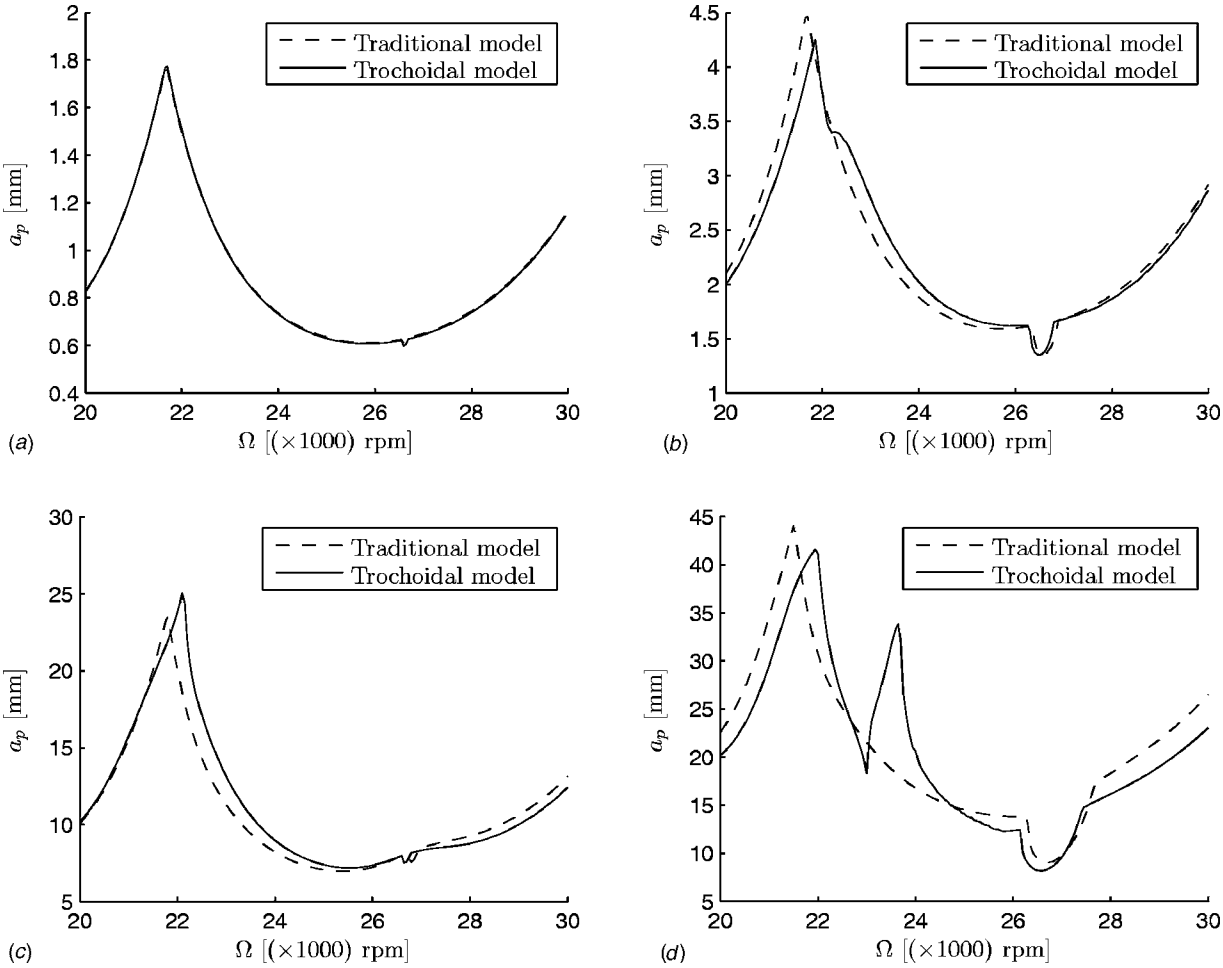

Fig. 13 Stability lobes for downmilling using the traditional and the trochoidal model for several immersion levels. (*a*) 100% immersion; (*b*) 50% immersion; (*c*) 10% immersion; (*d*) 5% immersion.

(i.e., a decrease of ϕ_e), which results in an increase of the stability limit. When a circular tooth path is assumed or when $x_F=1$, the periodic vibrations are not included in the equations that are used to calculate the stability. Therefore, this type of loss of contact is not included in these models.

Apart from this effect, the peak of the lobe shifts to the right for downmilling and to the left for upmilling. This effect is due to the periodic delay. This can be explained as follows. Chatter is caused by vibrations of the cutter on the tooth path. The location of the peaks of the SLD are defined by the ratio between the (dominant) natural frequency (causing the vibrations) of the machine-tool system and the tooth passing frequency (defining the tooth passing period). In one tooth passing period, $M+\epsilon$ waves exist on the workpiece where M is the number of full waves and $\epsilon<1$ the fraction of incomplete waves, see the upper part of Fig. 15.

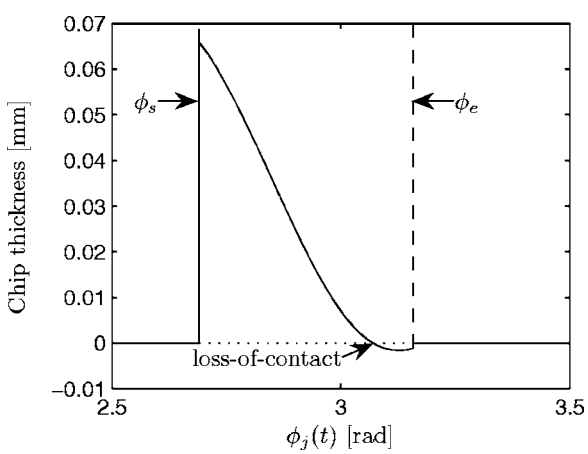

Fig. 14 Chip thickness including periodic vibrations for a 5% downmilling cut at 23,650 rpm and a_p=33 mm

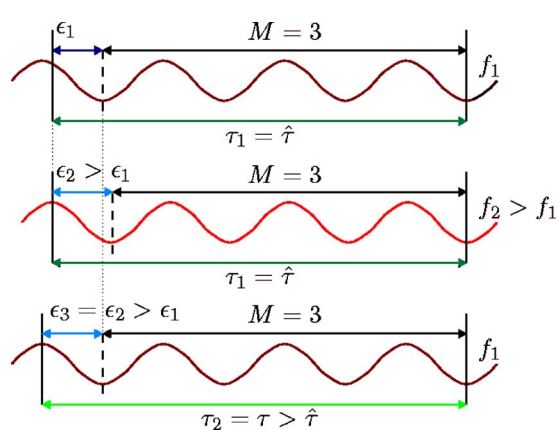

Fig. 15 Effect of the frequency change $f_1 \rightarrow f_2$ and the delay change $\tau_1 \rightarrow \tau_2$ on the fraction of waves ϵ_1 and $\epsilon_2=\epsilon_3$

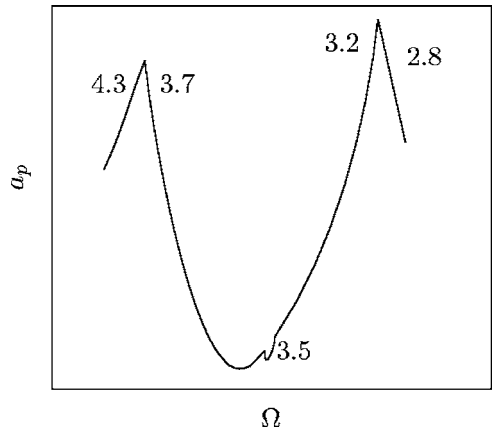

Fig. 16 Stability lobe with some possible values for the number of waves $M+\epsilon$

If the lobe of an SLD is followed from left to right for a system with a single natural frequency, the fraction ϵ of these waves decreases as is shown in Fig. 16. At the peak of a lobe, a jump is present to a wave where M is decreased by one, i.e., the number of waves goes, e.g., from 3.2 to 2.8. If the natural frequency of the system increases, more waves are generated in the tooth path for the same spindle speed (see the middle part of Fig. 15). This will cause the stability lobes to move to the right, since for the same spindle speed the fraction ϵ is increased ($\epsilon_2 > \epsilon_1$). For downmilling at 5%, the angles at which the cutter is engaged, lie close to π. As can be seen in Fig. 8, this gives a delay of about 1–1.5% higher than the constant delay $\hat{\tau}$. Therefore, the interval $t-\tau_j(t)$ is 1–1.5% larger than the interval $t-\hat{\tau}$, which allows 1–1.5% more waves to exist within this interval. This is depicted schematically in the lower part of Fig. 15 ($\epsilon_3 > \epsilon_1$). Hence, with increasing the delay, the same effect is achieved as with an increased natural frequency and the lobes move to the right in the case of low immersion downmilling. Similarly, the delay is lower than $\hat{\tau}$ for low immersion upmilling, which causes the peaks to move to the left.

6 Conclusions

Traditionally the tool path of a nonvibrating mill is modeled as a circular arc. In practice, the tool path is a trochoid. In modeling the milling process, the actual tool path influences the static chip thickness, the delay, and the entry and/or exit angles. Equations for the static chip thickness, the periodic delay, and the entry and exit angles have been derived using a trochoidal tool path. These models are more accurate than the models traditionally used.

An updated milling model has been constructed using these new equations. Hereafter, a nonlinear relation between the chip thickness and cutting force is taken into account in order to model the dependency of the stability limit to the chip load. The combination of the nonlinear cutting force model with the new tooth path model results in the fact that the periodic movement of the cutter needs to be calculated explicitly. The periodic solution of the model is found using the finite difference method. If this periodic solution is unstable (stable), it means that chatter does (not) occur. The limit of stability of the traditional model is compared to the limit of stability of the trochoidal model. To determine the stability of the periodic solution, the semi-discretization method is used for several radial immersion levels for both up- and downmilling. Results on the stability lobe diagram for low immersion cutting show that the stability limit of the trochoidal model differs significantly from that of the traditional model. More specifically, it is shown that using the trochoidal model for low radial immersion cuts, the peaks of the SLD move to the right for downmilling and to the left for upmilling compared to the traditional model due to the periodic delay. Moreover, due to the fact that the tool loses contact from the workpiece as a result of the periodic vibrations, extra peaks in the SLD can occur for low immersion cuts. For higher radial immersion rates, the differences between the two models decrease. This loss of contact cannot be predicted using a linear cutting force model.

From the simulation results, it can be concluded that for an accurate prediction of the stability lobes for low-immersion cutting it is necessary to drop the assumption that the tooth path is a circular arc. The tooth path should be modeled as a trochoid. For high immersion milling, the effect of the trochoidal tooth path model on the stability is negligible.

In future work, the stability lobes of both models will be validated by performing dedicated experiments.

Acknowledgment

This research is part of the TNO co-financing project Chattercontrol, which is supported in part by Jabro Tools, VDL ETG, and Somatech. The authors would like to thank N. J. Mallon for his help on the finite difference method.

References

[1] Tlusty, J., and Polacek, M., 1963, "The Stability of Machine Tools against Self-Excited Vibrations in Machining," *Proceedings ASME International Research in Production Engineering*, Pittsburgh, PA, pp. 465–474.
[2] Tobias, S. A., and Fishwick, W., 1958, "The Chatter of Lathe Tools Under Orthogonal Cutting Conditions," Trans. ASME, **80**, pp. 1079–1088.
[3] Davies, M. A., Pratt, J. R., Dutterer, B., and Burns, T. J., 2002, "Stability Prediction for Low Radial Immersion Milling," J. Manuf. Sci. Eng., **124**(2), pp. 217–225.
[4] Insperger, T., and Stépán, G., 2004, "Vibration Frequencies in High-Speed Milling Process or a Positive Answer to Davies Pratt, Dutterer, and Burns," J. Manuf. Sci. Eng., **126**(3), pp. 481–487.
[5] Stépán, G., Insperger, T., and Szalai, R., 2005, "Delay Parametric Excitation, and the Nonlinear Dynamics of Cutting Processes," Int. J. Bifurcation Chaos Appl. Sci. Eng., **15**(9), pp. 2783–2798.
[6] Szalai, R., and Stépán, G., 2006, "Lobes and Lenses in the Stability Chart of Interrupted Turning," ASME J. Comput. Nonlinear Dyn. **1**(3), pp. 205–211.
[7] Szalai, R., Stépán, G., and Hogan, S. J., 2004, "Global Dynamics of Low Immersion High-Speed Milling," Chaos, **14**(4), pp. 1069–1077.
[8] Altintas, Y., 2000, *Manufacturing Automation*, Cambridge University Press, Cambridge, UK.
[9] Insperger, T., Stépán, G., Bayly, P. V., and Mann, B. P., 2003, "Multiple Chatter Frequencies in Milling Processes," J. Sound Vib., **262**(2), pp. 333–345.
[10] Martellotti, M. E., 1941, "An Analysis of the Milling Process," Trans. ASME, **63**, pp. 677–700.
[11] Martellotti, M. E., 1945, "An Analysis of the Milling Process. Part 2. Down Milling," Trans. ASME, **67**, pp. 233–251.
[12] Li, H. Z., Liu, K., and Li, X. P., 2001, "A New Method for Determining the Undeformed Chip Thickness in Milling," J. Mater. Process. Technol., **113**, pp. 378–384.
[13] Spiewak, S., 1994, "Analytical Modeling of Cutting Point Trajectories in Milling," J. Eng. Ind., **116**, pp. 440–448.
[14] Spiewak, S., 1995, "An Improved Model of the Chip Thickness in Milling," CIRP Ann., **44**(1), pp. 39–42.
[15] Altintas, Y., and Budak, E., 1995, "Analytical Prediction of Stability Lobes in Milling," CIRP Ann., **44**(1), pp. 357–362.
[16] Insperger, T., and Stépán, G., 2004, "Updated Semi-Discretization Method for Periodic Delay-Differential Equations With Discrete Delay," Int. J. Numer. Methods Eng., **61**(1), pp. 117–141.
[17] Long, X. H., and Balachandran, B., 2004, "Milling Model With Variable Time Delay," *Proceedings ASME International Mechanical Engineering Congress and Exposition*, Anaheim, CA, November, Vol. 15, pp. 933–940.
[18] Faassen, R. P. H., van de Wouw, N., Oosterling, J. A. J., and Nijmeijer, H., 2003, "Prediction of Regenerative Chatter by Modelling and Analysis of High-Speed Milling," Int. J. Mach. Tools Manuf., **43**(14), pp. 1437–1446.
[19] Insperger, T., and Stépán, G., 2004, "Stability Analysis of Turning With Periodic Spindle Speed Modulation via Semi-discretization," J. Vib. Control, **10**, pp. 1835–1855.
[20] Insperger, T., Stépán, G., Hartung, F., and Turi, J., 2005, "State Dependent

Regenerative Delay in Milling Processes," *Proceedings ASME International Design Engineering Technical Conferences*, Long Beach, CA, September, Paper No. DETC2005-85282.
[21] Balachandran, B., 2001, "Nonlinear Dynamics of Milling Processes," Philos. Trans. R. Soc. London, **359**(1781), pp. 793–819.
[22] Nayfeh, A. H., and Balachandran, B., 1995, *Applied Nonlinear Dynamics, Analytical, Computational, and Experimental Methods*, Wiley-International, Chichester, UK.
[23] Parker, T. S., and Chua, L. O., 1989, *Practical Numerical Algorithms for Chaotic Systems*, Springer, Berlin, Germany.
[24] Faassen, R. P. H., van de Wouw, N., Oosterling, J. A. J., and Nijmeijer, H., 2005, "Updated Tool Path Modelling With Periodic Delay for Chatter Prediction in Milling," *Proceedings 5th Euromech Nonlinear Dynamics Conference (ENOC)*, Eindhoven, The Netherlands, August, Paper No. 08-109, pp. 1080–1089.